PROCEEDINGS A

royalsocietypublishing.org/journal/rspa

Research

Cite this article: Liu X, Tang T, Mostert W, Adcock TAA. 2025 Phase manipulation to analyse different types of nonlinearity using water waves as a case study. *Proc. R. Soc. A* **481**: 20240831.
https://doi.org/10.1098/rspa.2024.0831

Received: 29 October 2024
Accepted: 11 April 2025

Subject Areas:
ocean engineering, wave motion, fluid mechanics

Keywords:
nonlinear, phase manipulation, harmonics, signal separation, signal reconstruction

Author for correspondence:
X. Liu
e-mail: xinyu.liu2@eng.ox.ac.uk

Phase manipulation to analyse different types of nonlinearity using water waves as a case study

X. Liu, T. Tang, W. Mostert and T. A. A. Adcock

Department of Engineering Science, University of Oxford, Oxford, UK

XL, 0009-0003-2376-8899; TT, 0000-0002-6365-9342

We develop a phase-based manipulation technique, which can be adopted for many physical problems that involve separating the slave harmonics from the free waves. This technique extends the existing literature by developing a general solution to the problem while enabling the incorporation of arbitrary numbers and combinations of phases for computation. We further extend our matrix formulation to phase-based reconstruction applications, where a missing phase can be predicted from other phase-shifted signals with all slave harmonics included. This allows a clean separation between weakly nonlinear effects from the strong nonlinear process such as the breaking of water waves. We examine the possible sources for the phase-based reconstruction error, including the bandwidth of the input signal, the nonlinear effects, different phase combinations and phase misalignment. We aim to provide a reference for the optimal choice of the number and combination of phases to be selected. We use surface gravity-driven water waves as a case study.

1. Introduction

Harmonics of a fundamental frequency occur in many different situations. A classic example is an ideal pendulum. The linearized equations describe such a pendulum system with only one frequency. However, in the fully nonlinear regime, there will be harmonics at the odd integer multiples of this frequency [1,2].

THE ROYAL SOCIETY PUBLISHING

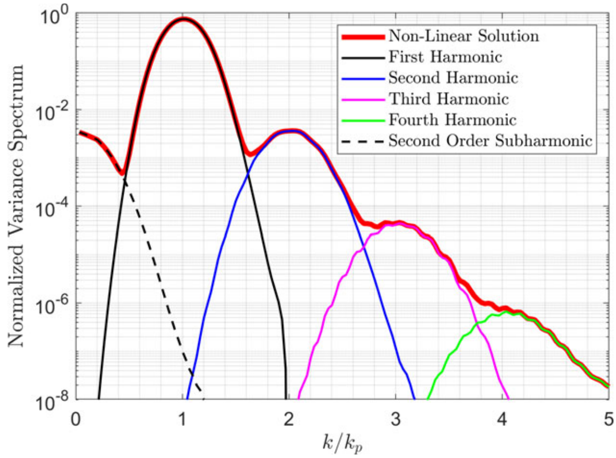

Figure 1. Normalized spectrum of the nonlinear signal, first, second, third and fourth harmonics and the second-order subharmonic at linear focus with steepness $Ak_p = 0.12$, where A is the amplitude of the fundamental frequency and k_p is the peak wavenumber. The bandwidth parameter for the input spectrum is $\alpha = 7$ (see details in equation (3.1)).

When waves propagate through nonlinear media, the amplitude and phase of the harmonics will be functions of the freely propagating components. Such harmonics are termed 'bound' or 'slave' harmonics.

This phenomenon is relevant to the study of surface gravity water waves, which is the primary focus of our paper, but it is also common to any broad-banded wave in nonlinear media. In surface gravity-driven waves, the difference between a crest and trough is often visible, and the corresponding mathematical treatment dates from the work of Stokes [3]. In the context of water waves, there are many reasons why we may need to separate the bound waves from the free waves. For example, to understand the bound wave contribution to a problem [4], or to analyse the bound waves because of what they tell us about the freely propagating waves [5] or to remove the bound waves from the analysis in order to better understand the freely propagating waves [6]. Harmonics of the fundamental signal structure will also be important in wave–structure interaction [7], and these harmonics are often more significant than those in the wave propagation problem.

For regular waves, or ones with a very narrow bandwidth, simple filtering in the Fourier domain is typically used. However, for broad banded waves, such as those found in the ocean, the spectra of bound and free waves overlap, making simple filtering less effective. An example of the spectrum of a wave group with moderate steepness is shown in figure 1, where overlaps between adjacent harmonics can be observed. For propagating waves, where information is known both in space and time, it is possible to filter using the known dispersion relationship [8], although this method does not always lead to clean separation, in practice [9].

An approach to separating different harmonics is to use different phases of the fundamental signal and then combine these together so as to lead to certain components cancelling, enabling simple filtering to be then applied. For instance, consider the simplest case of a wave with the mathematical structure

$$F_0 = A^2 f_{20} + A f_{11} \cos\varphi + A^2 f_{22} \cos 2\varphi + A^3 f_{33} \cos 3\varphi + A^4 f_{44} \cos 4\varphi + \mathcal{O}(A^5), \tag{1.1}$$

where F represent any wave signal with the structure described in equation (1.1), such as the surface elevation η, the velocity potential or hydrodynamic forces in the case of water waves. The subscript of F refers to the initial phase shift to the phase function φ, and A denotes the amplitude of the fundamental signals, while f_{mn} are the transfer functions that describe the relationship between wave amplitude and other physical quantities. For example, one such transfer function is

royalsocietypublishing.org/journal/rspa *Proc. R. Soc. A* **481**: 20240831

the force-amplitude transfer function [10,11]. Following in the convention within the community [6,10–13], the indices m and n represent the orders and the frequency/wavenumber of the bound harmonic, respectively. For instance, the term A^2f_{20} refers to the second-order subharmonic (difference interaction), while the remaining terms describe superharmonic (sum interaction). For clarity, the second-order subharmonic is the only subharmonic term shown here.

If one considers a signal whose initial phase is 180° out of phase (i.e. the fundamental signal is inverted), we get a signal

$$F_{180} = A^2f_{20} - Af_{11}\cos\varphi + A^2f_{22}\cos 2\varphi - A^3f_{33}\cos 3\varphi + A^4f_{44}\cos 4\varphi + \mathcal{O}(A^5). \tag{1.2}$$

The two signals can then be combined to give odd and even harmonics thus: $\eta_{\text{odd}} = (\eta_0 - \eta_{180})/2$ and $\eta_{\text{even}} = (\eta_0 + \eta_{180})/2$.

These make filtering much 'cleaner' as there is less overlap between higher-order harmonics. Here we call these equations as 'formulations', which manage to separate the harmonics through linear combinations of signals with different initial phase shifts. To our knowledge, this was introduced by Baldock *et al*. [6] and has been used widely ever since in ocean engineering. It has been extended to consider four phases [12] which allows signals to be organized sets of harmonics, e.g. $\{1st, 5th, 9th, \ldots\}$, $\{2nd, 6th, 10th \ldots\}$, etc., and thus facilitate better separation than with only two phases. Twelve phases have also been considered [13]. These techniques work well in an experimental or numerical setting where the phase of a fundamental signal can be controlled, although the approach fails if there is 'strong' nonlinearity such as wave-breaking where the structure of signal in equation (1.1) is no longer valid. With sufficient data, the technique can be applied to random signals by analysing the largest crests and troughs and assuming that on average the fundamental wave is of the same magnitude for both crests and troughs [14]. The approach has also been extended to consider waves interacting with structures that oscillate with their own harmonics [15]. The approach has also been applied in medical imaging [16].

A recent development involves using this approach to analyse 'strong' nonlinearities, such as the secondary load cycle in wave–structure interactions [7]. When only one or a few wave signals exhibit both weak and strong nonlinear behaviour, while the other wave signals experience only weak nonlinearities—such as four-wave interactions [17]—these other phases can be used to reconstruct the unseen phase where strong nonlinearity does not occur. This method effectively allows for a clear separation between the effects of strong nonlinearity on the physical phenomenon, isolating it from the weakly nonlinear effects.

The present paper aims to generalize this phase manipulation approach to arbitrary numbers and combinations of phases. This allows more flexibility in application, and potentially more accurate results. Firstly, we introduce a novel, although straightforward system of matrix analysis to calculate the formulations of phase-based separation. This allows us to extract different harmonics from an arbitrary number and combination of initial phases (including determining if this cannot be found). We then separate different harmonics of the original signal without using the original signal, and by adding them up, an unseen signal that contains only the weak nonlinearity of the original signal can be reconstructed. We then analyse the errors in the reconstruction, by comparing the reconstructed signal with the original signal, under different conditions such as input spectral bandwidth, number of phases, nonlinear effects and combination of phases. We use a case study of the propagation of deep water waves to test our phase manipulation approach under various wave conditions.

2. Methods

(a) Generalization of the phase-based separation method

In the present work, we aim to extend the previous phase-based separation approach [6,12,13]. We manage to systematically generate formulations for arbitrary combinations and number of phases with a novel matrix manipulation approach.

royalsocietypublishing.org/journal/rspa Proc. R. Soc. A 481: 20240831

Our new method starts by constricting information of free and bound waves in equations (1.1) and (1.2) into cosine and sine harmonic, as shown in the phase coefficient matrix **A**,

$$\mathbf{A} = \begin{bmatrix} \cos(\boldsymbol{N} \otimes \boldsymbol{\Theta}) \\ \sin(\boldsymbol{N} \otimes \boldsymbol{\Theta}) \end{bmatrix}, \tag{2.1}$$

where $\boldsymbol{N} = (1, 2, \ldots, n)^{\mathrm{T}}$ represents the order vector where n is the highest harmonic of interest, the superscript T is the transpose operator, and $\boldsymbol{\Theta} = (\theta_1, \theta_2, \ldots, \theta_n)$ as the initial phase shift vector. For instance, in equations (1.1) and (1.2) the order vector would be $\boldsymbol{N} = \{1, 2, 3, 4\}^{\mathrm{T}}$, and the initial phase shift vector will be $\boldsymbol{\Theta} = (0, 180)$. Here $\boldsymbol{N} \otimes \boldsymbol{\Theta}$ results in a $n \times n$ matrix, and the cos is performed on each element in this matrix. See an example in equation (2.5).

We can further augment the phase coefficient matrix **A** by using the Hilbert transform to create signals with a shift of 90° in phase. Further discussion on the influence of the Hilbert transform is shown in appendix A, where we find that this does not compromise the analysis. After incorporating the Hilbert transform, the phase coefficient matrix can be augmented as

$$\mathbf{A} = \begin{bmatrix} \cos(\boldsymbol{N} \otimes \boldsymbol{\Theta}) & : & -\sin(\boldsymbol{N} \otimes \boldsymbol{\Theta}) \\ \sin(\boldsymbol{N} \otimes \boldsymbol{\Theta}) & : & \cos(\boldsymbol{N} \otimes \boldsymbol{\Theta}) \end{bmatrix}, \tag{2.2}$$

where the elements on the right-hand side of the dashed line represent the cosine and sine harmonics of the Hilbert-transformed signals. Note that $\mathbf{A} \in \mathbb{R}^{2n \times 2n}$ is a $2n \times 2n$ matrix.

The next step is to formulate the target harmonic matrix **b**. Ideally, we aim to leave only a single harmonic, which leads to the form

$$\mathbf{b} = \begin{bmatrix} \mathbf{I}_{n \times n} \\ \mathbf{0}_{n \times n} \end{bmatrix} = \underbrace{\begin{bmatrix} 1 & 0 & \cdots & 0 \\ 0 & 1 & \cdots & 0 \\ \vdots & & \ddots & \\ 0 & 0 & \cdots & 1 \\ \hdashline 0 & 0 & \cdots & 0 \\ 0 & 0 & \cdots & 0 \\ \vdots & & \ddots & \\ 0 & 0 & \cdots & 0 \end{bmatrix}}_{n}. \tag{2.3}$$

Here $\mathbf{I}_{n \times n}$ is a $n \times n$ square identity matrix, and $\mathbf{0}_{n \times n}$ is a $n \times n$ square zero matrix. The elements over the dashed line correspond to the cosine harmonics, and those below the dashed line correspond to the sine harmonics. $b \in \mathbb{R}^{2n \times n}$ is a $2n \times n$ matrix.

Then the solution matrix, i.e. a matrix of what proportion of each run should be used in the separation, **x** can be formulated by considering

$$\mathbf{A}\mathbf{x} = \mathbf{b}, \tag{2.4}$$

where each row of the solution matrix **x** corresponds to a single harmonic.

To better illustrate the method in the present paper, an example of the classical four-phase separation described in [12] is presented in equation (2.5). Note here that now the order vector $\boldsymbol{N} = (1, 2, 3, 4)^{\mathrm{T}}$ and $\boldsymbol{\Theta} = (0°, 90°, 180°, 270°)$.

$$\underbrace{\begin{array}{c} \\ C_1 \\ C_2 \\ C_3 \\ C_4 \\ S_1 \\ S_2 \\ S_3 \\ S_4 \end{array}\begin{array}{c} \begin{array}{cccccccc} F_0 & F_{90} & F_{180} & F_{270} & F_0^H & F_{90}^H & F_{180}^H & F_{270}^H \end{array} \\ \left[\begin{array}{cccc:cccc} 1 & 0 & -1 & 0 & 0 & -1 & 0 & 1 \\ 1 & -1 & 1 & -1 & 0 & 0 & 0 & 0 \\ 1 & 0 & -1 & 0 & 0 & 1 & 0 & -1 \\ 1 & 1 & 1 & 1 & 0 & 0 & 0 & 0 \\ \hdashline 0 & 1 & 0 & -1 & 1 & 0 & -1 & 0 \\ 0 & 0 & 0 & 0 & 1 & -1 & 1 & -1 \\ 0 & -1 & 0 & 1 & 1 & 0 & -1 & 0 \\ 0 & 0 & 0 & 0 & 1 & 1 & 1 & 1 \end{array}\right] \end{array}}_{\text{Phase Coefficient Matrix } \mathbf{A}} \underbrace{\begin{array}{c} F_0 \\ F_{90} \\ F_{180} \\ F_{270} \\ F_0^H \\ F_{90}^H \\ F_{180}^H \\ F_{270}^H \end{array}\left[\begin{array}{cccc} \frac{1}{4} & \frac{1}{4} & \frac{1}{4} & \frac{1}{4} \\ 0 & -\frac{1}{4} & 0 & \frac{1}{4} \\ -\frac{1}{4} & \frac{1}{4} & -\frac{1}{4} & \frac{1}{4} \\ 0 & -\frac{1}{4} & 0 & \frac{1}{4} \\ 0 & 0 & 0 & 0 \\ -\frac{1}{4} & 0 & \frac{1}{4} & 0 \\ 0 & 0 & 0 & 0 \\ \frac{1}{4} & 0 & -\frac{1}{4} & 0 \end{array}\right]}_{\text{Solution Matrix } \mathbf{x}} = \overbrace{\begin{array}{c} C_1 \\ C_2 \\ C_3 \\ C_4 \\ S_1 \\ S_2 \\ S_3 \\ S_4 \end{array}\left[\begin{array}{cccc} 1 & 0 & 0 & 0 \\ 0 & 1 & 0 & 0 \\ 0 & 0 & 1 & 0 \\ 0 & 0 & 0 & 1 \\ 0 & 0 & 0 & 0 \\ 0 & 0 & 0 & 0 \\ 0 & 0 & 0 & 0 \\ 0 & 0 & 0 & 0 \end{array}\right]}^{\text{Target Harmonic Matrix } \mathbf{b}} \tag{2.5}$$

where C_n denotes the cosine harmonics, S_n denotes the sine harmonics, F_θ denotes wave signals with different initial phase shift θ, and superscript H denotes the Hilbert transform. Here the row vector in $\mathbf{x}$ corresponds to the row vector in $\mathbf{b}$, as indicated by their colour.

Now the formulation for the four-phase separation is given in the solution matrix $\mathbf{x}$, while the proportion of each run with different initial phases is labelled on the left-most column. Translating the above formulations to those previously used in the literature [12] gives

$$\begin{aligned} \boxed{\frac{F_0 - F_{90}^H - F_{180} + F_{270}^H}{4}} &= A f_{11}\cos\varphi + A^3 f_{31}\cos\varphi + O(A^5), \\ \boxed{\frac{F_0 - F_{90} + F_{180} - F_{270}}{4}} &= A^2 f_{22}\cos 2\varphi + A^4 f_{42}\cos 2\varphi + O(A^6), \\ \boxed{\frac{F_0 + F_{90}^H - F_{180} - F_{270}^H}{4}} &= A^3 f_{33}\cos 3\varphi + O(A^5), \\ \boxed{\frac{F_0 + F_{90} + F_{180} + F_{270}}{4}} &= A^2 f_{20} + A^4 f_{44}\cos 4\varphi + O(A^6). \end{aligned} \tag{2.6}$$

Note that here F denote the wave signal and f is the transfer function in [12]. We use F in the present paper for consistency with [12]. It should be noted that F can be any quantities of interest with a Stokes-type structure, like the surface elevation η, the hydrodynamics forces, the free surface velocity potential, etc. In addition, our method also allows obtaining the order of accuracy in the separation (the $O(A^5)$ in equation (2.6) (so as in equation (2.8) or equation (2.11)) from the matrix operation. One can augment the rows of phase coefficient matrix $\mathbf{A}$, then times the solution matrix, then there will be additional rows in the new target harmonic matrix. Non-zero elements in the nth row indicate the presence of nth harmonic in the formulation. Consequently, the order of accuracy of the formulation can be evaluated.

We now consider the least number of phases needed to separate nth harmonic, and from the matrix calculation, it is obvious that n phases are sufficient for a single harmonic in the formulation up to nth harmonic.

(b) Phase-based reconstruction

The effectiveness of the phase-based reconstruction technique leverages the fact that phase-based separation does not require the original signal. We can use the separated harmonics as the source terms to 'reconstruct' an unseen signal from signals with different initial phase shifts.

The novel matrix manipulation framework proposed in §2a can also be applied straightforwardly for the reconstruction problem, where the only modification required is to set the phase coefficient vectors in matrix A corresponding to the original signal and Hilbert-transformed original signal as zero. An example of the evenly distributed three-phase (i.e.

$(90^\circ, 180^\circ, 270^\circ)$) reconstruction, as first described in [7] is shown in equation (2.7), where the modification is emphasized with the red box.

$$\underbrace{\begin{array}{c} \\ C_1 \\ C_2 \\ C_3 \\ S_1 \\ S_2 \\ S_3 \end{array}\!\!\begin{array}{c} \begin{array}{cccccccc} F_0 & F_{90} & F_{180} & F_{270} & F_0^H & F_{90}^H & F_{180}^H & F_{270}^H \end{array} \\ \left[\begin{array}{cccc:cccc} 0 & 0 & -1 & 0 & 0 & -1 & 0 & 1 \\ 0 & -1 & 1 & -1 & 0 & 0 & 0 & 0 \\ 0 & 0 & -1 & 0 & 0 & 1 & 0 & -1 \\ \hdashline 0 & 1 & 0 & -1 & 0 & 0 & -1 & 0 \\ 0 & 0 & 0 & 0 & 0 & -1 & 1 & -1 \\ 0 & -1 & 0 & 1 & 0 & 0 & -1 & 0 \end{array}\right] \end{array}}_{\text{Phase Coefficient Matrix}\quad \mathbf{A}} \underbrace{\begin{array}{c} F_0 \\ F_{90} \\ F_{180} \\ F_{270} \\ F_0^H \\ F_{90}^H \\ F_{180}^H \\ F_{270}^H \end{array}\!\!\left[\begin{array}{ccc} 0 & 0 & 0 \\ -\frac{1}{4} & -\frac{1}{2} & -\frac{1}{4} \\ -\frac{1}{2} & 0 & -\frac{1}{2} \\ -\frac{1}{4} & -\frac{1}{2} & -\frac{1}{4} \\ 0 & 0 & 0 \\ -\frac{1}{4} & 0 & \frac{1}{4} \\ 0 & 0 & 0 \\ \frac{1}{4} & 0 & -\frac{1}{4} \end{array}\right]}_{\text{Solution Matrix}\quad \mathbf{x}} = \underbrace{\begin{array}{c} C_1 \\ C_2 \\ C_3 \\ S_1 \\ S_2 \\ S_3 \end{array}\!\!\left[\begin{array}{ccc} 1 & 0 & 0 \\ 0 & 1 & 0 \\ 0 & 0 & 1 \\ 0 & 0 & 0 \\ 0 & 0 & 0 \\ 0 & 0 & 0 \end{array}\right]}_{\text{Target Harmonic Matrix } \mathbf{b}} \tag{2.7}$$

If we write the formulation in the solution matrix $\mathbf{x}$ into the traditional form, we will have

$$-\frac{1}{4}\left(\boxed{F_{90} + 2F_{180} + F_{270} + F_{90}^H - F_{270}^H}\right) = -A^2 f_{20} + A f_{11} \cos\varphi - A^4 f_{44} \cos 4\varphi + \mathcal{O}\left(A^5\right), \tag{2.8a}$$

$$-\frac{1}{2}\left(\boxed{F_{90} + F_{270}}\right) = -A^2 f_{20} + A^2 f_{22} \cos 2\varphi - A^4 f_{44} \cos 4\varphi + \mathcal{O}\left(A^6\right), \tag{2.8b}$$

and $$-\frac{1}{4}\left(\boxed{F_{90} + 2F_{180} + F_{270} - F_{90}^H + F_{270}^H}\right) = -A^2 f_{20} + A^3 f_{33} \cos 3\varphi + A^4 f_{44} \cos 4\varphi + \mathcal{O}(A^7). \tag{2.8c}$$

Now the first, second and third harmonics of F_0 have been separated in equations (2.8*a*) to (2.8*c*), respectively, without using F_0, and the separation for the second-order subharmonic will be introduced in equation (2.12). We can readily reconstruct the unseen signal of F_0 which only undergoes weak nonlinearity by

$$F_{0-\text{weak-nonlinearity}} = A^2 f_{20} + A f_{11} \cos\varphi + A^2 f_{22} \cos 2\varphi + A^3 f_{33} \cos\varphi + \mathcal{O}(A^4). \tag{2.9}$$

Then, by comparing the difference between the F_0 that undergo both strong and weak nonlinearity, and $F_{0-\text{weak-nonlinearity}}$, we should be able to separate the strong nonlinearity from the weak nonlinearity.

It should be noted here that the formulation for the first- equation (2.8*a*) and second-order equation (2.8*b*) harmonics are identical to the formulations in [7], while there is a difference in the third order. Tang *et al.* gives

$$\frac{1}{2}(-F_{90}^H + F_{270}^H) = A f_{11} \cos\varphi - A^3 f_{33} \cos 3\varphi + A^5 f_{55} \cos 5\varphi + \mathcal{O}(A^7), \tag{2.10}$$

which is an alternative way to reconstruct the third harmonic, by frequency filtering on the odd harmonics. In this study, we adopt the formulation in equation (2.8*c*) because the 'frequency smearing' from lower harmonics tends to cause more significant contamination compared with higher harmonics. If overlap is unavoidable, we prefer it from the higher harmonics, as their contamination is relatively smaller.

Although an equally distributed phase combination $(90^\circ, 180^\circ, 270)$ is selected in this example, arbitrary phase combinations can be used in phase-based reconstruction as developed below, and the effects of unevenly distributed phase combinations are discussed in §4d.

We now discuss the fewest number of phases needed to reconstruct the nth harmonics. Similar to the number of phases required in phase separation, n phases are needed to reconstruct nth harmonics. In other words, n phases are sufficient to ensure that, up to the nth harmonic, only a single harmonic appears in the formulation. Similarly, higher harmonic ($n + 4$ for four-phase) may exist in the formulation, and frequency filtering can then be applied to remove the contamination from higher harmonics.

(c) Orthogonal separation for the second-order subharmonic

We now move on to the separation of the second-order subharmonic, which is important for applications such as wave-following measurement buoys [18], floating offshore wind turbines [19] and field data analysis [20]. In the current phase-based reconstruction, extra efforts are needed as there can be an extra second-order subharmonic contribution in the formulations of all harmonics. For instance, an example of the unevenly distributed three-phase (i.e. $135^\circ, 225^\circ, 255^\circ$) reconstruction in equation (2.11). Frequency filtering can be applied to remove the second-order subharmonic in the formulations of higher harmonics, see in [7], but it cannot tackle the second-order subharmonic contribution in the first harmonic, due to the frequency overlap as shown in figure 1. An orthogonal separation approach for the second-order subharmonic is presented here:

$$\boxed{-0.35F_{135} - 0.35F_{225} - 0.97F_{255} + 0.2F^H_{135} + 1.32F^H_{225} - 0.56F^H_{255}}$$
$$= -1.67A^2 f_{20} + 0.96A^2 f^H_{20} + A f_{11}\cos\varphi + \mathcal{O}\left(A^4\right), \tag{2.11a}$$

$$\boxed{-1.37F_{255} + 0.79F^H_{135} + 1.37F^H_{255} - 0.79F^H_{255}}$$
$$= -1.37A^2 f_{20} + 1.37A^2 f^H_{20} + A^2 f_{22}\cos 2\varphi + \mathcal{O}\left(A^4\right), \tag{2.11b}$$

and

$$\boxed{0.35F_{135} + 0.35F_{225} - 0.97F_{255} + 0.2F^H_{135} + 1.32F^H_{225} - 0.56F^H_{225}}$$
$$= -0.27A^2 f_{20} + 0.96A^2 f^H_{20} + A^3 f_{33}\cos 3\varphi + \mathcal{O}(A^4). \tag{2.11c}$$

Our orthogonal separation method is based on the orthogonality of the Hilbert transform and the assumption that the second-order subharmonic will not change with the phase manipulation. The second-order subharmonic can be separated by solving

$$\begin{bmatrix} A^2 f_{20} \\ A^2 f^H_{20} \end{bmatrix} = \begin{bmatrix} c_1 & c_2 \\ -c_2 & c_1 \end{bmatrix}^{-1} \begin{bmatrix} S \\ S^H \end{bmatrix}, \tag{2.12}$$

where S is the formulation to separate the nth (ideally $n > 1$) harmonics, superscript H denotes the Hilbert transform and $A^2 f_{20}$ denotes the second-order subharmonic. Low-pass filtering is then applied to remove the contamination from higher harmonics. The sum coefficients c_1 and c_2 can be readily evaluated from equation (2.11), as the sum of the solution vector for the non-Hilbert-transformed signals and that for the Hilbert-transformed signals, respectively. Take the first harmonic in equation (2.11*a*) as an example. Now the c_1 is the sum of the coefficient before non-Hilbert transformed signals, which is $c_1 = -0.35 - 0.35 - 0.97 = -1.67$, while c_2 is that for the Hilbert transformed signals, namely $c_2 = 0.2 + 1.32 - 0.56 = 0.96$.

To examine the accuracy of the aforementioned orthogonal separation method, we compare the second-order subharmonic from the orthogonal separation against that from the four-phase separation [12], using wave groups based on a fully nonlinear potential flow solver (see details in §3). Here orthogonal separation is performed in the formulation of the third harmonics, in a three-phase reconstruction in equation (2.8). A low-pass frequency filter is applied here at $2k_p$ (preserving more than 99% of the energy), to ensure a fair comparison of the second-order subharmonic.

Here the normalized error is defined as

$$\text{Normalized Error} = \frac{g_1 - g_2}{\max(g_1)}, \tag{2.13}$$

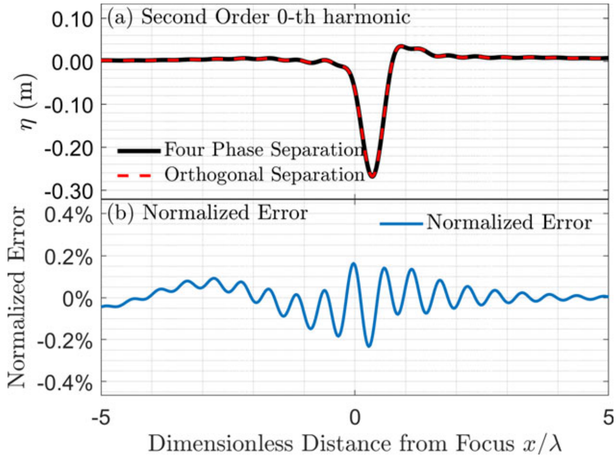

Figure 2. Comparison of the second-order subharmonic from four-phase separation [12] and orthogonal separation shown in equation (2.12) with a steepness of 0.18 at $t = 5T_p$ when the error reaches its maximum. The difference normalized by the maximum absolute value of the second-order subharmonic, as defined in equation (2.13), between them is shown in percentage in (b). A low-pass frequency filter is applied at $2k_p$.

where g_2 signal is compared with g_1 signal here. The maximum error in the orthogonal separation method is illustrated in figure 2, and it can be observed that these two methods give similar results, where the maximum difference is no more than 1%.

3. Numerical experiment

The methods described in this paper have a general applicability to a range of problems. However, the method was first applied to the propagation of water waves and this remains one of the key applications. As such we choose water wave propagation to test the tools developed above.

We run a fully nonlinear potential flow solver OCEANWAVE3D [21,22], a software tool for simulating large-scale surface flow over variable depths in coastal and offshore engineering application. To examine the accuracy of the proposed phase-based and reconstruction method, we generate uni-directional focused wave groups with a semi-Gaussian spectrum given by

$$S(k) = \begin{cases} \exp\left(\dfrac{-(k-k_\mathrm{p})^2}{2k_\mathrm{l}^2}\right), & \text{if } k < k_p \\ \exp\left(\dfrac{-(k-k_\mathrm{p})^2}{2k_\mathrm{r}^2}\right), & \text{if } k > k_p, \end{cases} \tag{3.1}$$

where k is the wavenumber, k_p is the peak wavenumber, k_l and k_r is the initial spectral bandwidth for the low-wavenumber and high-wavenumber range of the spectrum (divided by k_p), respectively. Here $k_l = 0.004606$ and $k_r = k_p(2\log(10)^\alpha)^{1/2}$. We use the parameter α to control the energy distribution in the high-wavenumber tails thus changing the spectral bandwidth of the spectrum, by specifying $10^{-\alpha}$ at $2k_p$. For instance, $\alpha = 1$ means the energy at $2k_p$ is 0.1 times the energy at the peak wavenumber. A larger α value corresponds to less energy in the tail and a narrow-banded spectrum, whereas a smaller α indicates a broad-banded spectrum.

Such a spectrum allows us to adjust the energy distribution on the high-wavenumber tail directly, and the energy distribution will directly affect the quality of the reconstruction of the wave profile and higher harmonics as shown in the later studies in §4a,b. For low-wavenumber range, we choose $k_l = 0.004608$, following [23], which approximately corresponds to $\alpha = 8$. As shown by Gibbs & Taylor [23], $\alpha = 8$ is an approximation to JONSWAP with $\gamma = 3.3$, and $\alpha = 1$ is

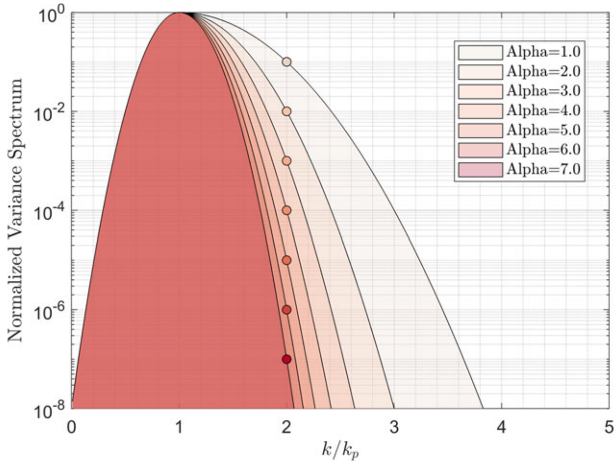

Figure 3. Normalized semi-Gaussian spectrum used in this study. The alpha value controls the spectral bandwidth. The value of k_l is set approximately to correspond to $\alpha = 8$.

an approximation to the Pierson–Moskowitz spectrum [24]. The bandwidth range in the present paper should cover the bandwidth for most realistic waves. A semi-Gaussian spectrum that is normalized by its own peak energy is shown in figure 3.

We then obtain the initial condition consisting of the free surface elevation and the velocity potential based on linear theory as

$$\left.\begin{aligned} \eta(x,t) &= \sum_{n=1}^{N} a_n \cos[k_n(x-x_c)-\omega_n(t-t_c)+\theta_i] \\ \text{and} \quad \phi(x,z,t) &= \sum_{n=1}^{N} a_n \frac{\omega_n}{k_n} \frac{\cosh k_n(z+h)}{\sinh k_n h} \sin[k_n(x-x_c)-\omega_n(t-t_c)+\theta_i], \end{aligned}\right\} \tag{3.2}$$

where η is the surface elevation, ϕ is the velocity potential, a_n is the amplitude of the nth component, ω_n is the angular frequency, k_n is the wavenumber, t_c is the focused time, x_c is the focused position, θ_i is the initial phase shift, which is the component of Θ in §2a, z is the vertical coordinate and h is the water depth. We use $N = 2000$ as the number of spectral components, which is sufficient to resolve the spectrum. All the simulations are initialized at $t = -20T_p$ before linear focus and end at $t = 40T_p$ after linear focus, where T_p is the peak period.

We specify the surface elevation and velocity potential at each location in space and let the wave group propagate. We include higher-order correction up to the fifth order to reduce the error wave effects. We employ the exact second-order correction based on the second-order wave theory by Dalzell [25]. We approximate higher-order corrections following [9,26].

Information regarding numerical discretization is included in table 1. And we have performed convergence tests on spatial-temporal discretization and reversibility, and the effectiveness of the higher order corrections following [9,21,22].

4. Analysis of accuracy

In this section, we begin by examining the impact of the bandwidth on the reconstruction of the unseen signal, as discussed in §4a. Here the reconstruction of the unseen signal means using the method in §2b and equation (2.9) to estimate the signals that only undergo weak nonlinearity. We then explore the role of the number of phases in relation to the accuracy of the reconstruction in §4b, as to avoid unnecessary costs of obtaining signals with different initial phase shifts. Following this, we delve into the nonlinear focusing effects in §4c. Finally, we investigate the

Table 1. Summary of the numerical set-up. Here L_x is the length of the computational domain which is long enough to avoid waves hitting the boundary. N_x is the number of the grids in the x-axis. Δx is the spatial resolution, and λ is the wavelength calculated based on peak period. T_{total} is the duration of our simulation, here equal to $60T_p$, where T_p is the peak period. Δt is the temporal resolution, and h is the water depth. In our cases, $k_pd = 4.185$. N_z is the number of grids in the vertical coordinate. The Courant–Friedrichs–Lewy number is defined by $\mathrm{CFL} = c_g \cdot \Delta t/\Delta x$, where c_g is the group velocity.

L_x(m)	N_x	Δx(m)	$\lambda/\Delta x$	T_{total}(s)	T_p(s)	Δt(s)	$T_p/\Delta t$	h(m)	N_z	CFL
23 028	4097	5.62	40	720	12	0.4	30	150	45	0.67

optimal selection of phase combinations for reconstruction, as detailed in §4d, and the stability of the phase reconstruction to phase misalignment in the experiment in §4e. In this section, in order to make a fair comparison for nth harmonics, frequency filtering is applied where necessary. For the first harmonic, low-pass filtering is applied to remove higher harmonics in the formulation, while the orthogonal separation is used to remove the second-order subharmonic in §2c. For second and higher harmonics, band pass filtering is applied. For nth harmonics ($n > 1$), band pass filter is applied from $(n-1)k_p$ to $(n+2)k_p$.

(a) Effects of spectral bandwidth

The phase-based reconstruction technique in the present paper requires the separation of different harmonics in the spectral domain. Thus, a large spectral bandwidth might increase the reconstruction error due to the increased overlap between the adjacent orders of harmonics—the so-called 'frequency smearing effects' in [12]. As such, we discuss how the bandwidth effects in the spectrum might influence the reconstruction of the unseen signal.

We first investigate the effects of the spectral bandwidth on the reconstruction of the unseen signal, when using three-, five-, seven- and eleven-phase reconstructions. Here all the phase-based reconstructions employ evenly distributed phase combinations, and $n-1$ phase reconstruction means using a phase combination of $(360^\circ/n, 2\times 360^\circ/n, \ldots, (n-1)\times 360^\circ/n)$. For instance, three-phase reconstruction means using a phase combination of $(90^\circ, 180^\circ, 270^\circ)$ to reconstruct the unseen signal at phase 0 (i.e. no phase shift). Reconstruction based on unevenly distributed phases will be discussed separately in §4d. The input spectral bandwidth is controlled by the bandwidth parameter α (see details in equation (3.1)). Increasing α means decreasing the input spectral bandwidth. A steepness of $Ak_p = 0.02$ minimizes nonlinear dispersion effects—this is the steepness the wave group would be at focus under linear evolution.

We present the reconstruction error on the unseen signal for different initial bandwidths in figure 4a, where we use the surface similarity parameter Q [27] to describe the differences between the reconstructed signals and the original ones. This surface similarity parameter Q is defined as

$$Q(f_1, f_2) = \frac{\left(\int |\mathcal{F}_1(k) - \mathcal{F}_2(k)|^2\,\mathrm{d}k\right)^{1/2}}{\left(\int |\mathcal{F}_1(k)|^2\,\mathrm{d}k\right)^{1/2} + \left(\int |\mathcal{F}_2(k)|^2\,\mathrm{d}k\right)^{1/2}}, \tag{4.1}$$

where f_1 and f_2 are the signals to be compared, f_1 is the reference signal, $\mathcal{F}_1$ and $\mathcal{F}_2$ are their complex Fourier components. The surface similarity parameter is a metric that measures the difference in phase and amplitude, and varies between zero (for perfect agreement) and one (for perfect disagreement). Other error metrics were considered (e.g. root mean square error, the cosine similarity, the absolute maximum difference, etc.) but we believe that the surface similarity parameter is the most appropriate error metric since it compares the information in both the amplitude and the phase, and its results seem consistent with the visual investigation of errors.

The results depicted in figure 4a demonstrate an increase in reconstruction error with increasing bandwidth for cases where $\alpha < 2$. Notably, the error associated with the three-phase

royalsocietypublishing.org/journal/rspa Proc. R. Soc. A 481: 20240831

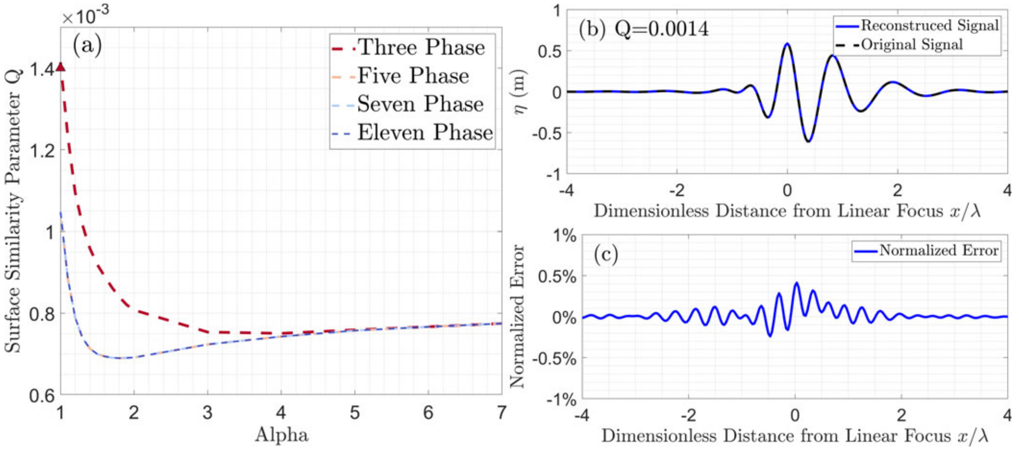

Figure 4. (a) Time-averaged surface similarity parameter Q of the total wave profiles for the different initial bandwidths of the spectrum (see details in equation (3.1)). The initial steepness Ak_p is 0.02 to minimize the nonlinear focusing effects. We also present a comparison between the three-phase reconstruction signal and the original signal in (b), where $\alpha = 1$ and the surface similarity parameter Q is 0.0013. Their normalized error (see equation (2.13)) is presented in (c).

reconstruction is significantly larger compared with that observed in the five-, seven- and 11-phase reconstructions. The discrepancies among the latter are negligible. This arises because the three-phase reconstruction, as detailed in equation (2.8*c*), lacks a sufficient number of phases to separate the third harmonic cleanly from the fourth harmonic. Consequently, the fourth harmonic contaminates the third-order region, an effect that becomes increasingly severe as the bandwidth increases. See the wave profile of the reconstruction error in figure 4c for reference. For narrow-banded wave groups, as illustrated in figure 4 for cases where $\alpha > 3$, the reconstruction errors associated with the three-, five-, seven-, and 11-phase methods are nearly identical indicating that even the simplest three-phase manipulation has been effective at removing any overlap. Thus, for many ocean applications (where bandwidths are relatively narrow), three-phase reconstruction is sufficient particularly given that, even for the most extreme case considered, the error is small enough for most applications.

In addition, we compare the reconstructed signal obtained from the three-phase reconstruction with the original signal in figure 4b, alongside their corresponding normalized error shown in figure 4c. This comparison establishes a link between Q and the percentage error in the wave profile. Specifically, it is observed that $Q = 0.0014$, as indicated by the red triangle in figure 4a, corresponds to a maximum difference in the wave profile of less than 0.5%.

(b) Effects of number of phases

In this section, we delve deeper into the influence of the number of phases on the reconstruction of higher harmonics, given that the difference in the overall wave profile is relatively small. In addition, we examine how many phases are sufficient for phase-based reconstruction, beyond which increasing the number of phases no longer improves performance. This analysis is key to optimizing the phase-based reconstruction while minimizing the additional costs associated with acquiring signals with different initial phase shifts.

We quantify the reconstruction error of the first five harmonics using the surface similarity parameter Q. The ground truth for different harmonics is extracted by four-phase separation, and these errors are presented in bar charts in figure 5, comparing different numbers of phases. As discussed in §2b, the three-phase reconstruction struggles to capture the fourth- and fifth-harmonics. To use the three-phase reconstruction as a benchmark, we implement a simplified two-phase formulation with frequency filtering for both the fourth (in equation (2.8*b*)) and fifth

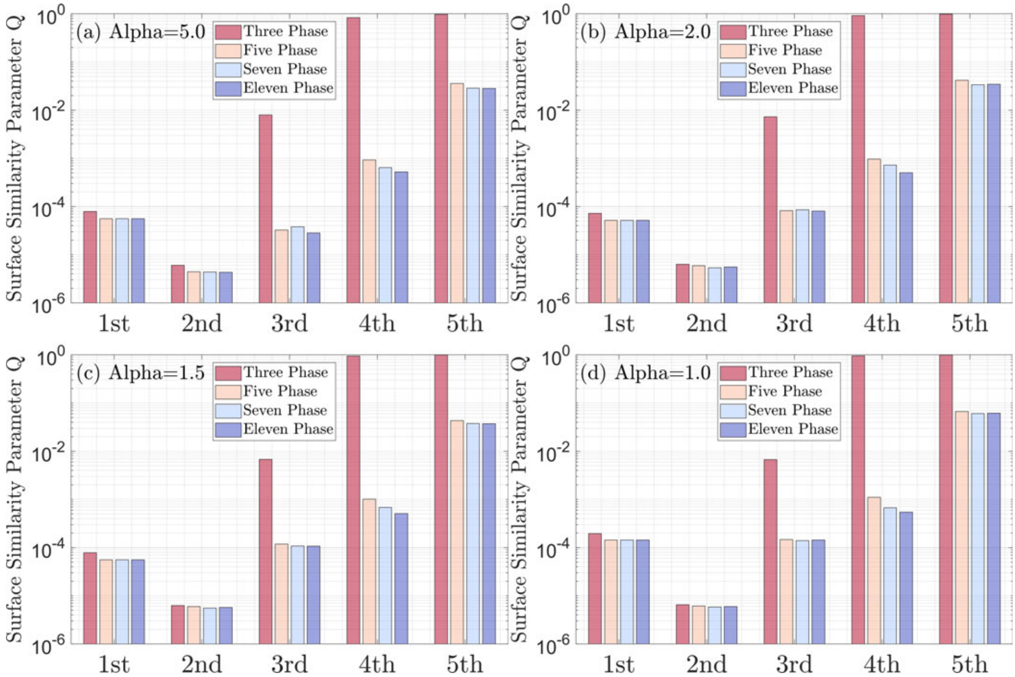

Figure 5. Time-averaged surface similarity parameter Q of the first five harmonics (as indicated in the x-axis as first to fifth) by the different number of phases at four different bandwidth parameter $\alpha = 5, 2, 1.5$ and 1 in (a,b,c,d), respectively. The initial steepness Ak_p is 0.02 to eliminate the nonlinear focusing effects.

(in equation (2.10)) harmonics. Figure 5 contains four subplots showing the reconstruction errors across different bandwidths. The bandwidth parameter α is indicated in the top-left corner of each subplot.

As shown in figure 5, the five-phase reconstruction consistently outperforms the three-phase reconstruction across all harmonics, with the advantage being particularly pronounced for the fourth and fifth harmonics. Specifically, we observe that the surface similarity parameter Q for the three-phase reconstruction approaches 1 (indicating perfect disagreement) for the fourth and fifth harmonics, while the five-phase reconstruction yields Q values that remain small. In addition, a progressive breakdown of the three-phase reconstruction is evident as we move from the first to the fifth harmonic. For the first and second harmonics, all phase-based reconstructions exhibit comparable performance. However, starting with the third harmonic, the three-phase reconstruction shows a noticeable increase as it cannot distinguish the third and fourth harmonics (see equation (2.8*c*)). This failure becomes more pronounced at the fourth and fifth harmonics, where the three-phase reconstruction breaks down.

However, increasing the number of phases beyond five does not result in significant improvements in reconstruction accuracy. This phenomenon can be attributed to the fact that only the first five harmonic orders are considered in the present analysis, and five phases are sufficient to reconstruct a single harmonic. Therefore, we recommend that the number of phases to use should be based on the highest harmonic of interest, which helps to minimize unnecessary costs associated with obtaining additional signals with different initial phase shifts.

The effects of bandwidth appear to have minimal influence on the number of phases required for accurate reconstruction. No clear trend is observed with increasing bandwidth, although a slight increase in the value of Q can be recognized as the input bandwidth increases. To link the bandwidth parameter to a realistic ocean spectrum, the $\alpha = 8$ is an approximation of JONSWAP with $\gamma = 3, 3$ used by Gibbs & Taylor [23], and $\alpha = 1$ is an approximation to P-M spectrum [24]. The bandwidth range tested in §4a,b encompasses the most realistic broad-banded waves found

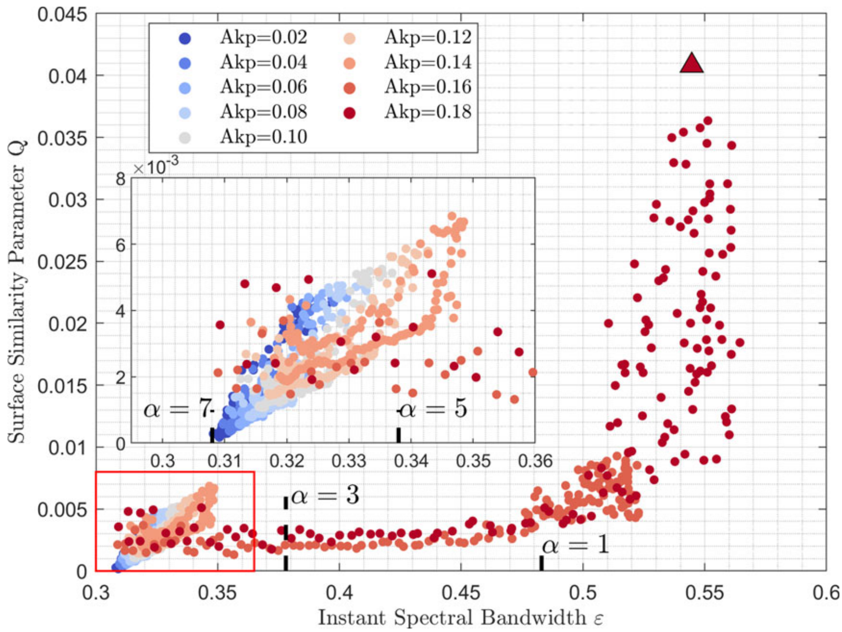

Figure 6. Surface similarity parameter Q versus the instant spectral bandwidth ϵ with different initial input steepness. The Q here is calculated based on the first harmonic at different time steps, with the definition of ε, and that is why we term the bandwidth as instant. The input spectral bandwidth is $\alpha = 7$ to minimize the bandwidth effects. The instant spectral bandwidth ϵ corresponding to our bandwidth parameter $\alpha = (1, 3, 5, 7)$ defined in equation (3.1) are labelled. The subplot is a local enlargement of the red box. The triangles in the plot correspond to the error in wave profile in figure 7.

in the ocean if one excludes bimodal sea states. We thus conclude that the bandwidth effects, within realistic sea states, do not substantially alter the relationship between the number of phases and the reconstruction error for higher harmonics with a sufficient number of phases, given that there is no visible difference between five, seven and 11 phases.

(c) Realistic extreme waves

In the previous section, we chose to analyse very small waves to assess the impact of bandwidth directly, as the bandwidth is unchanged over the simulation. However, the size of the higher harmonics will also be small. We now turn to more nonlinear simulations; in these, the higher harmonics are more realistic but the bandwidth change due to nonlinear dispersion can no longer be ignored. We present the three-phase reconstruction error versus the instant spectral bandwidth ε in figure 6 at various steepness. Here the input spectral bandwidth is $\alpha = 7$, and the instant spectral bandwidth ϵ is calculated based on the first harmonic at different timesteps following [28] $\varepsilon = (1 - (m_2^2/m_0m_4))^{1/2}$, where m_n is the nth spectral moment.

We begin by recapping the nonlinear effects on the width of the wave group of initially dispersed wave groups which can be thought of as a change in the local bandwidth [29–31] (who built on earlier work such as [32]). A clear trend emerges: cases with higher steepness exhibit larger instant spectral bandwidths, particularly for steepness values exceeding $Ak_p = 0.16$. Specifically, for moderate steepness values of $Ak_p = 0.14$ or lower, nonlinear effects tend to expand the spectral bandwidth from its initial value of $\alpha = 7$ to around $\alpha = 5$. However, for wave groups with steepness greater than $Ak_p = 0.16$, the spectral bandwidth can easily expand, and the α would go up to 1 and even extend beyond that. Here we observe this bandwidth increase in the spatial domain.

We now turn our attention to the reconstruction error arising from nonlinear effects. As mentioned earlier in §4a, higher bandwidth generally leads to an increase in reconstruction

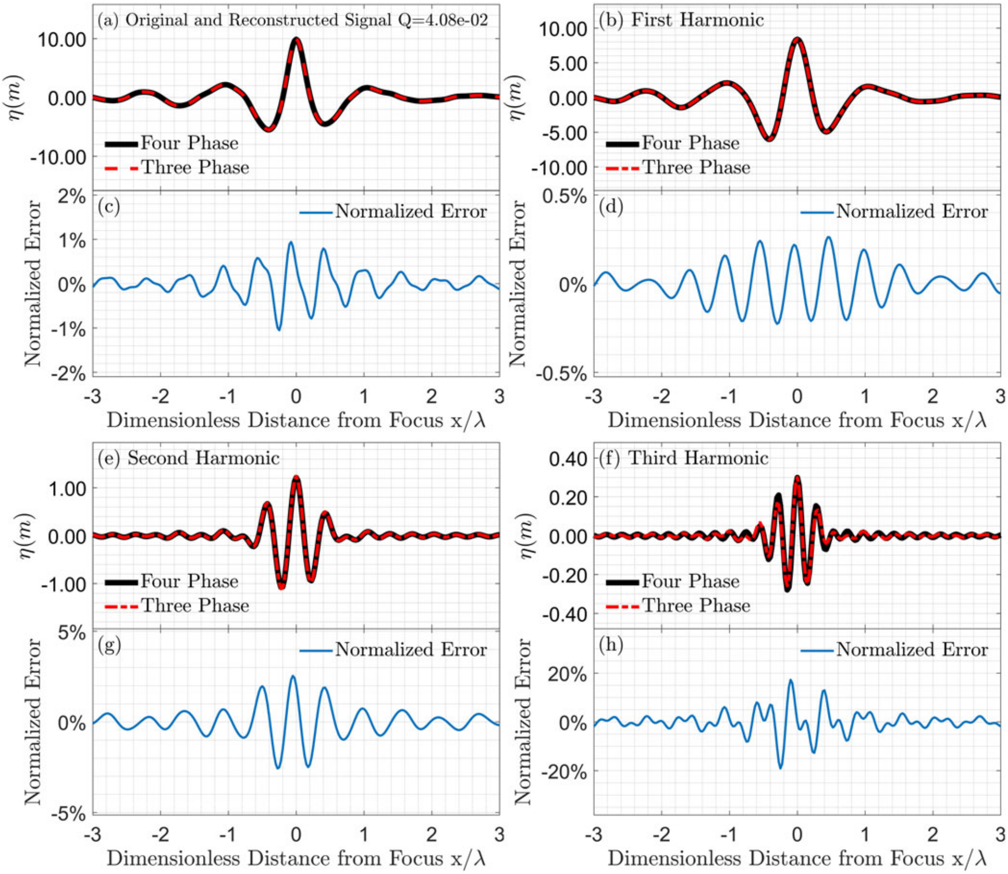

Figure 7. Comparison of the first (b), second (e) and third harmonics (f) of the reconstructed signal (a) between four-phase separation and three-phase reconstruction. We present the wave profiles at $Ak_p = 0.18$ when $t = 9.1T_p$ when the reconstruction error reaches its maximum, where the similarity value is given at the corner corresponding to the red triangle in figure 6. The normalized percentage error between four-phase separation and three-phase reconstruction is presented in (c,d,g,h) below each harmonic.

error, given that frequency filtering becomes less effective when the harmonic regions overlap. For moderate steepness values of $Ak_p = 0.14$ or lower, nonlinear effects induce only mild reconstruction errors, with the maximum value of Q in this regime being approximately 7×10^{-3}. However, at higher steepness values, particularly for $Ak_p = 0.16$ or greater, nonlinear effects become more pronounced, and the reconstruction error increases significantly with bandwidth. Specifically, the maximum Q for $Ak_p = 0.16$ reaches around 0.01, while for $Ak_p = 0.18$, it rises to approximately 0.04 (as labelled by the red triangle in figure 6)—several times larger than the error observed at lower steepness levels, and the corresponding error in wave profile percentage will be presented in figure 7.

To visualize the maximum reconstruction error due to nonlinear effects, we present the first-, second- and third harmonics of the reconstructed signal in figure 7, where the Q value here is labelled in the red triangle in figure 6. The harmonics derived from the four-phase separation method [12] are used as the ground truth. The reconstruction error remains relatively small, with the unseen signal exhibiting an error of approximately 1%. However, it is noteworthy that the reconstruction error for the third harmonic is significantly larger, around 20%, highlighting the challenge of accurately reconstructing higher harmonics with three-phase reconstruction under nonlinear effects. Generally, our results support those in §4b. This also highlights that in choosing

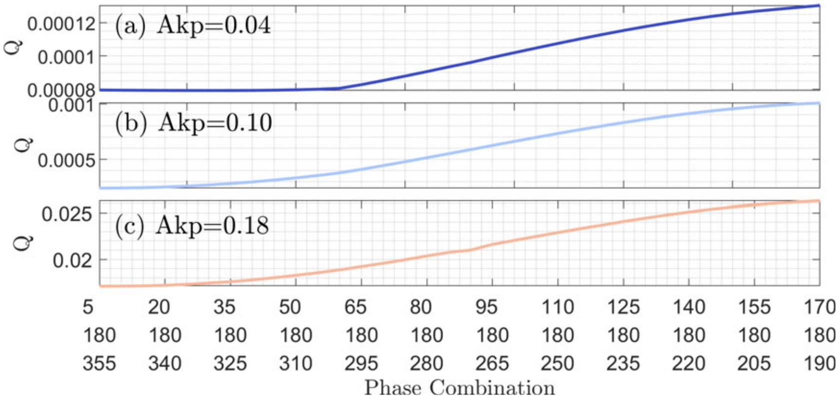

Figure 8. Time-averaged surface similarity parameter Q of the overall wave profiles with different phase combinations. Cases with different initial steepness are also presented herein (a–c).

the number of phases required for reconstruction, not only the input bandwidth but also the maximum bandwidth should be considered.

(d) Effects of phase combinations

The rationale behind the proposed phase-based reconstruction technique is that strong nonlinearity may occur in only one or a few specific phases, while the remaining phases experience only weak nonlinear effects. We can leverage that fact to reconstruct an unseen signal that predominantly undergoes weak nonlinear processes, thereby isolating the strong nonlinearity. In this context, it is reasonable to infer that the phase corresponding to 180° is the least likely to exhibit strong nonlinearity, while signals with smaller phase shifts are more prone to strong nonlinear effects. Thus, evenly distributed phases, which are used in [7], are not always achievable, especially as the number of phases increases. For instance, it is difficult and time-consuming to get parameters exactly right so that wave breaking occurs in only one phase. Therefore, it becomes essential to evaluate the reconstruction error across different phase combinations in order to ensure the robustness and accuracy of the phase-based reconstruction method.

We present the reconstruction error versus different phase combinations in figure 8 for various steepness. The input spectral bandwidth is set to $\alpha = 7$ to minimize the bandwidth effects. In this analysis, we fix the 180° phase, which is the least likely to experience strong nonlinearity. We then pair it with symmetric phases around 180°, progressively narrowing the phase pair from (i.e. 5°, 180°, 355°) to (i.e. 175°, 180°, 185°).

We observe a limited increase in the reconstruction error with the narrowing of the phase combination in figure 8. When the phase combination gets narrower, the phase coefficient matrix $\mathbf{A}$ (see §2a) becomes ill conditioned, and the coefficient in the solution matrix $\mathbf{x}$ will increase and might lead to a larger reconstruction error. However, even for an extreme case where we have phases of 170°, 180° and 190° the error remains small and is likely to be much lower than errors in real experimental measurements. This is constant across all steepness, although only three steepness is presented here. Note that as discussed in §4c, the maximum bandwidth is dependent on steepness.

(e) Stability to phase misalignment

The numerical simulations used in this study enable us to control the phase very accurately. However, in other applications, this might not be so either because of issues with the signal generation, the timing of the measurement system, or from the inherent physics in the problem

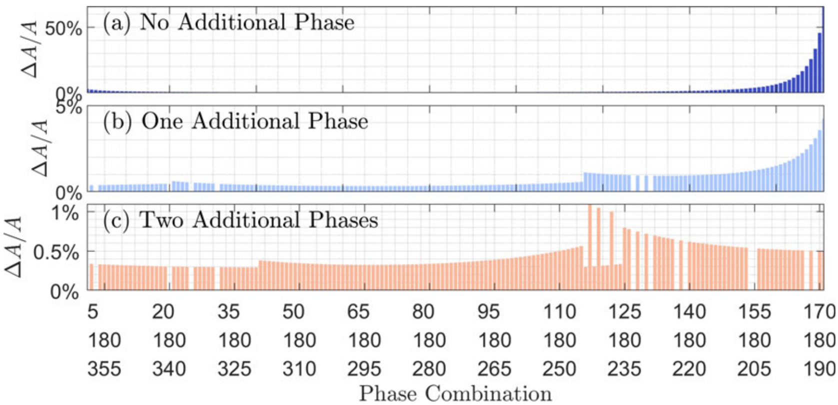

Figure 9. Maximum relative envelope difference $\Delta A/A$ of phase-based reconstruction error under a small phase misalignment with no, one and two additional phases, plotted in (a–c), respectively. $\Delta A = 0$ in figure 9 (b,c) indicates that the phase with misalignment is not used in that phase combination.

as one phase travels at a slightly different speed to another. Understanding the sensitivity to this is important particularly as we have noted that our solution matrix $\mathbf{x}$ becomes increasingly ill conditioned. This occurs when the phase combination in §4d approaches 180°. In this section, we further investigate this error introduced by a small phase misalignment and explore the potential strategies to mitigate its effects.

To explore this consider a small phase misalignment ϵ in just the initial phase F_0. Under the limits that $\epsilon \to 0$, we have $\cos(\epsilon) = 1$ and $\sin(\epsilon) = \epsilon$. The phase with misalignment F_0' in equation (1.1), and its Hilbert transformed version $F_0^{H\prime}$ can be written as

$$\left.\begin{aligned} & F_0' = Af_{11}(\cos\varphi + \epsilon\sin\varphi) + \mathcal{O}(A^2), \\ \text{and} \qquad & F_0^{H\prime} = Af_{11}(\sin\varphi + \epsilon\cos\varphi) + \mathcal{O}(A^2). \end{aligned}\right\} \tag{4.2}$$

Getting the coefficients a_1 and a_2 for F_0 and F_0^H, respectively, from the solution matrix $\mathbf{x}$, the contribution of the phase misalignment ϵ can be written as

$$\Delta A = \epsilon\sqrt{a_1^2 + a_2^2}\sin\left(\varphi + \arctan\frac{a_2}{a_1}\right). \tag{4.3}$$

In figure 9a–c, we present the change of the amplitude ΔA compared with the first harmonic amplitude A with $\epsilon = 1°$, under various phase combinations. It is shown in figure 9a that the error caused by phase misalignment is relatively small for most of the combinations, which indicates such misalignment has minimal effect on our method.

When the combination nears 180°, the error grows significantly, which indicates that for an ill-conditioned matrix that is close to 175°, 180°, 185°, phase misalignment will likely lead to more error. As such extreme combinations should be avoided during experiments where imperfect timing is suspected. However, in figure 9b,c, by adding one or two additional phases (namely use four-, five-phase reconstruction), the error caused by phase misalignment is significantly smaller indicating that a practical mitigation method to such a problem is to perform extra experiments with different phases. $\Delta A = 0$ in figure 9b,c indicates that the phase with misalignment is not used in that phase combination.

5. Discussion and conclusion

The phase separation approach introduced by Baldock *et al.* [6] has been used for nearly 30 years and with various modifications and extensions. The present paper generalizes the method and introduces a simple but effective way of determining coefficients for arbitrary combinations of phases. We further explore the phase reconstruction method as an extrapolation using rotational symmetry to recreate a missing phase. We acknowledge that in the presence of strong nonlinearity in the missing phase, the reconstructed solution is not a physically valid solution given an unbroken wave of these dimensions cannot exist. We go on to analyse the effectiveness of the method, in particular, showing that provided there is minimal overlap between harmonics, there is no reason to add additional phases. We also show that accurate results are possible with a wide range of phase combinations, which may therefore be chosen for experimental convenience, and add extra flexibility to the approach. In experiments where exact phase control is challenging, we have shown that extra phases can stabilize the phase reconstruction to phase misalignment.

The key problem with the approach that still remains intractable is the '31' problem (see $A^3 f_{31} \cos\varphi$ in equation (2.6) and [33,34] for reference). The same goes for 42 components as well as higher harmonics. Though these subharmonic terms will not contribute to the reconstruction error in the present work, it should be acknowledged that what is separated is still the first harmonics, but still contains higher-order components. In addition, the phase-based separation and reconstruction inherently require that all phases are similarly dispersive. This means that there will be some limitations of our method in shallow water where triad interactions become dominant. Applications of the general approach to shallower depths include Taylor *et al.* [35], who examined wave loading on a cylinder using four-phase separation at $k_p d = 0.88$, demonstrating that phase separation remains valid at this depth as well as Hunt [36], who prove that phase separation can work in the coastal zone until wave overturning. The phase-based separation/reconstruction can be used to investigate some wave–structure interaction, such as inertia loading [7,37,38]. However, there are also forms of nonlinearity that do not appear to be straightforward to analyse with phase separation. The most obvious of these are the harmonics that arise from friction which has the classic $|u|u$ form where u is velocity for Morison drag [39].

The methods developed in this paper have broad potential applications across various domains in nonlinear wave physics, as their underlying assumptions are not restricted to specific types of waves. For mechanical waves (i.e. sound waves, seismic waves, water waves, etc.) as a common type of wave, the phase of the harmonics also depends on the fundamental frequency. The present phase-based manipulation might have the potential to improve the quality of ultrasound imaging and harmonic imaging [16], by separating higher harmonics. It might also be used in the reconstruction of the seismic wave [40], given that our methods essentially can be applied in arbitrary numbers and phase shifts. For nonlinear optics, where the phases of the harmonics depend not only on the fundamental frequency but also on the polarization, the present method might provide guidance in the phase matching [41] in polarization response [42], which is critical to laser generation. In the context of water waves, the phase-based reconstruction has been used to investigate the effects of the secondary load cycle in wave–structure interaction [7], and we expect it to retrieve non-breaking signals and separate the wave-breaking effects, shedding light on the onset mechanisms of highly nonlinear wave breaking and exploring the associated energy dissipation processes. While the phase-based reconstruction approach in relation to wave-breaking has been central to this study, we recognize that other potential uses of reconstruction methods may not have been fully explored. For instance, errors in laboratory or numerical experiments can sometimes lead to missing phases, and the current technique can be used to check or replace these data without repeating the whole experiment.

Data accessibility. Find the initial conditions of the nonlinear waves used in this study at https://github.com/Xinyu01091002/Phase-manipulation-to-analyse-different-types-of-non-linearity-using-water-waves-as-a-case-study.

Also data is available from the Zenodo repository [43].

Declaration of AI use. We have not used AI-assisted technologies in creating this article.

Authors' contributions. X.L.: conceptualization, data curation, methodology, software, validation, visualization, writing—original draft, writing—review and editing; T.T.: conceptualization, data curation, methodology, project administration, software, supervision, visualization, writing—review and editing; W.M.: project administration, supervision, visualization, writing—review and editing; T.A.A.A.: conceptualization, project administration, supervision, visualization, writing—review and editing.

royalsocietypublishing.org/journal/rspa Proc. R. Soc. A 481: 20240831

All authors gave final approval for publication and agreed to be held accountable for the work performed therein.

Conflict of interest declaration. We declare we have no competing interests.

Funding. T.T. received support through Schmidt Sciences, LLC.

Acknowledgements. We thank Prof Paul Taylor (UWA) and Dr Thobani Hlophe (Oxford) for their input into this work.

Appendix A. Effects of using the Hilbert transform in analysis

The use of the Hilbert transform, as first introduced in the four-phase separation [12], can halve the numerical or experimental cost of obtaining extra signals. Hence, it would be of great importance to check whether there would be any differences caused by using the Hilbert transform, and how large these differences would be.

We compare the difference between the four-phase separation with the Hilbert transform and the 12-phase separation without the Hilbert transform, developed by the methods in §2a. We present the difference caused by using the Hilbert transform on the first-, second- and third-order harmonics of the signals in figure 10. We take a snapshot of the wave group at $A_k p = 0.18$ and $t = 9.1T_p$ when the difference caused by the Hilbert transform reaches its maximum.

It can be observed that the difference in the signals, in the first and second harmonics are much less than 0.5%. Even in the third harmonic where the error is the maximum among all, the

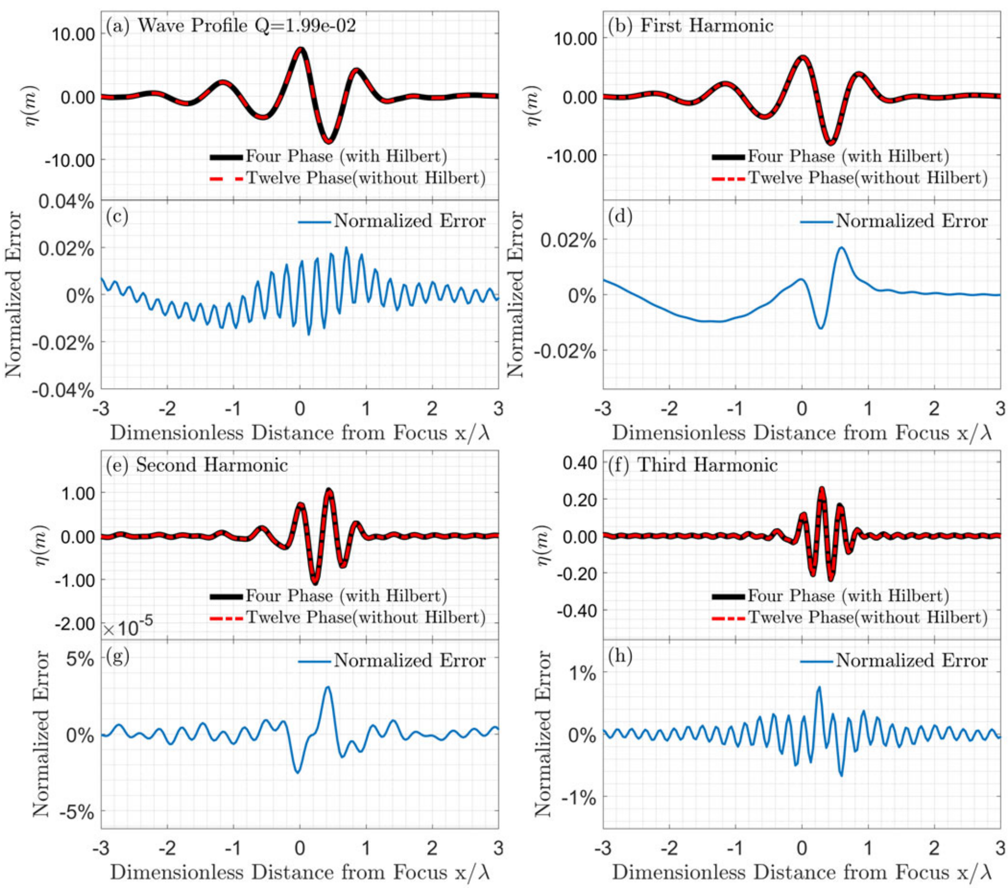

Figure 10. Comparison of the first (b), second (e) and third harmonics (f) of the signal (a) between four-phase separation with the Hilbert transform and the 12-phase separation without the Hilbert transform. We present the wave profiles at $Ak_p = 0.18$ when $t = 9.1T_p$ when the difference caused by using the Hilbert transform reaches its maximum. The normalized percentage error between four-phase separation and 12-phase separation is presented in (c, d, g, h) below each order of harmonics.

difference is still reasonably acceptable, which is no more than 1%. Therefore, we recommend using the Hilbert transform in phase-based separation and reconstruction, given that it can halve the cost of obtaining extra signals, and the difference caused by using the Hilbert transform is insignificant.

References

1. French AP. 2017 *Vibrations and waves*, 1st edn. Boca Raton, FL: CRC Press.
2. Nekorkin VI. 2015 *Introduction to nonlinear oscillations*, 1st edn. New York, NY: Wiley.
3. Stokes GG. 2009 *Mathematical and physical papers*, vol. 1. Cambridge, UK: Cambridge University Press.
4. Forristall GZ. 2000 Wave crest distributions: observations and second-order theory. *J. Phys. Oceanogr.* **30**, 1931–1943. (doi:10.1175/1520-0485(2000)030<1931:WCDOAS>2.0.CO;2)
5. Adcock TAA, Taylor PH. 2009 Estimating ocean wave directional spreading from an Eulerian surface elevation time history. *Proc. R. Soc. A* **465**, 3361–3381. (doi:10.1098/rspa.2009.0031)
6. Baldock TE, Swan C, Taylor PH. 1996 A laboratory study of nonlinear surface waves on water. *Phil. Trans. R. Soc. Lond. A* **354**, 649–676. (doi:10.1098/rsta.1996.0022)
7. Tang T, Ding H, Dai S, Taylor PH, Zang J, Adcock TAA. 2024 An experimental study of a quasi-impulsive backwards wave force associated with the secondary load cycle on a vertical cylinder. *J. Fluid Mech.* **994**, A9. (doi:10.1017/jfm.2024.648)
8. Slunyaev A, Kokorina A. 2019 The method of spectral decomposition into free and bound wave components. Numerical simulations of the 3D sea wave states. In *Geophysical Research Abstracts, Vienna, Austria*, vol. 21. EGU General Assembly 2019, Abstract EGU 2019-546.
9. Barratt D, Bingham HB, Adcock TAA. 2020 Nonlinear evolution of a steep, focusing wave group in deep water simulated with Oceanwave3D. *J. Offshore Mech. Arct. Eng.* **142**, 21201. (doi:10.1115/1.4044989)
10. Tan B, Orszaghova J, Wolgamot H, Kurniawan A, Todalshaug J. 2024 Third-order first-harmonic wave excitation forces on spherical geometries. In *Proc. 39th Int. Workshop on Water Waves and Floating Bodies, St Andrews, UK*. Abstract No. 42.
11. Kim Y, Kim J, Kim M. 1997 First- and second-order wave forces on a large spar platform. In *Proc. 7th Int. Offshore and Polar Engineering Conference (ISOPE), Chalottetown, Canada*. Paper no. ISOPE-I-97-034.
12. Fitzgerald CJ, Taylor PH, Eatock Taylor R, Grice J, Zang J. 2014 Phase manipulation and the harmonic components of ringing forces on a surface-piercing column. *Proc. R. Soc. A* **470**, 20130847. (doi:10.1098/rspa.2013.0847)
13. Hann M, Greaves D, Raby A. 2014 A new set of focused wave linear combinations to extract non-linear wave harmonics. In *Proc. 29th Int. Workshop on Water Waves and Floating Bodies, Osaka, Japan*, pp. 61–64.
14. Mj D, McAllister ML, Bredmose H, Adcock TAA, Taylor PH. 2023 Harmonic structure of wave loads on a surface piercing column in directionally spread and unidirectional random seas. *J. Ocean Eng. Marine Energy* **9**, 415–433. (doi:10.1007/s40722-022-00276-5)
15. Wolgamot H, Orszaghova J, Kurniawan A, Taylor PH, Todalshaug JH. 2023 Phase-manipulation with multiple controlled inputs to enhance investigation of nonlinear hydrodynamic effects. In *Proc. 38th Int. Workshop on Water Waves and Floating Bodies, Ann Arbor, MI*.
16. Tranquart F, Grenier N, Eder V, Pourcelot L. 1999 Clinical use of ultrasound tissue harmonic imaging. *Ultrasound Med. Biol.* **25**, 889–894. (doi:10.1016/S0301-5629(99)00060-5)
17. Phillips OM. 1960 On the dynamics of unsteady gravity waves of finite amplitude part 1. The elementary interactions. *J. Fluid Mech.* **9**, 193–217. (doi:10.1017/S0022112060001043)
18. McAllister ML, Van Den Bremer TS. 2019 Lagrangian measurement of steep directionally spread ocean waves: second-order motion of a wave-following measurement buoy. *J. Phys. Oceanogr.* **49**, 3087–3108. (doi:10.1175/JPO-D-19-0170.1)
19. Orszaghova J, Taylor PH, Wolgamot HA, Madsen FJ, Pegalajar-Jurado AM, Bredmose H. 2021 Wave- and drag-driven subharmonic responses of a floating wind turbine. *J. Fluid Mech.* **929**, A32. (doi:10.1017/jfm.2021.874)
20. Adcock TAA, Taylor PH, Yan S, Ma QW, Janssen PAEM. 2011 Did the draupner wave occur in a crossing sea? *Proc. R. Soc. A* **467**, 3004–3021. (doi:10.1098/rspa.2011.0049)

21. Engsig-Karup A, Bingham H, Lindberg O. 2009 An efficient flexible-order model for 3D nonlinear water waves. *J. Comput. Phys.* **228**, 2100–2118. (doi:10.1016/j.jcp.2008.11.028)
22. Bingham HB, Zhang H. 2007 On the accuracy of finite-difference solutions for nonlinear water waves. *J. Eng. Math.* **58**, 211–228. (doi:10.1007/s10665-006-9108-4)
23. Gibbs RH, Taylor PH. 2005 Formation of walls of water in 'fully' nonlinear simulations. *Appl. Ocean Res.* **27**, 142–157. (doi:10.1016/j.apor.2005.11.009)
24. Pierson WJ, Moskowitz L. 1964 A proposed spectral form for fully developed wind seas based on the similarity theory of S. A. Kitaigorodskii. *J. Geophys. Res.* **69**, 5181–5190. (doi:10.1029/JZ069i024p05181)
25. Dalzell J. 1999 A note on finite depth second-order wave–wave interactions. *Appl. Ocean Res.* **21**, 105–111. (doi:10.1016/S0141-1187(99)00008-5)
26. Walker DAG, Taylor PH, Eatock Taylor R. 2004 The shape of large surface waves on the open sea and the draupner new year wave. *Appl. Ocean Res.* **26**, 73–83. (doi:10.1016/j.apor.2005.02.001)
27. Perlin M, Bustamante MD. 2016 A robust quantitative comparison criterion of two signals based on the sobolev norm of their difference. *J. Eng. Math.* **101**, 115–124. (doi:10.1007/s10665-016-9849-7)
28. Holthuijsen LH. 2007 *Waves in oceanic and coastal waters*. Cambridge, UK: Cambridge University Press.
29. Gibbs R. 2004 Walls of water on the open ocean. PhD thesis, University of Oxford, UK.
30. Adcock TAA, Taylor PH. 2009 Focusing of unidirectional wave groups on deep water: an approximate nonlinear Schrödinger equation-based model. *Proc. R. Soc. A* **465**, 3083–3102. (doi:10.1098/rspa.2009.0224)
31. Adcock TAA, Taylor PH. 2016 Non-linear evolution of uni-directional focussed wave-groups on a deep water: a comparison of models. *Appl. Ocean Res.* **59**, 147–152. (doi:10.1016/j.apor.2016.05.012)
32. Lo E, Mei CC. 1985 A numerical study of water-wave modulation based on a higher-order nonlinear Schrödinger equation. *J. Fluid Mech.* **150**, 395–416. (doi:10.1017/S0022112085000180)
33. Madsen PA, Fuhrman DR. 2012 Third-order theory for multi-directional irregular waves. *J. Fluid Mech.* **698**, 304–334. (doi:10.1017/jfm.2012.87)
34. El-Dib Y. 2000 Instability of parametrically second- and third-subharmonic resonances governed by nonlinear Shrödinger equations with complex coefficients. *Chaos, Solitons Fractals* **11**, 1773–1787. (doi:10.1016/S0960-0779(99)00085-5)
35. Taylor P, Tang T, Adcock T, Zang J. 2024 Transformed-FNV: wave forces on a vertical cylinder — a free-surface formulation. *Coastal Eng.* **189**, 104454. (doi:10.1016/j.coastaleng.2024.104454)
36. Hunt A. 2002 Extreme waves, overtopping and flooding at sea defences. PhD thesis, University of Oxford, UK.
37. Tang T, Ryan G, Ding H, Chen X, Zang J, Taylor PH, Adcock TAA. 2024 A new Gaussian process based model for non-linear wave loading on vertical cylinders. *Coastal Eng.* **188**, 104427. (doi:10.1016/j.coastaleng.2023.104427)
38. Feng X, Taylor PH, Dai S, Day AH, Willden RHJ, Adcock TAA. 2020 Experimental investigation of higher harmonic wave loads and moments on a vertical cylinder by a phase-manipulation method. *Coastal Eng.* **160**, 103747. (doi:10.1016/j.coastaleng.2020.103747)
39. Morison J, Johnson J, Schaaf S. 1950 The force exerted by surface waves on piles. *J. Petroleum Technol.* **2**, 149–154. (doi:10.2118/950149-G)
40. Bianchin L, Forte E, Pipan M. 2019 Acoustic impedance estimation from combined harmonic reconstruction and interval velocity. *Geophysics* **84**, R385–R400. (doi:10.1190/geo2018-0296.1)
41. Franken PA, Hill AE, Peters CW, Weinreich G. 1961 Generation of optical harmonics. *Phys. Rev. Lett.* **7**, 118–119. (doi:10.1103/PhysRevLett.7.118)
42. Bloembergen N, Pershan PS. 1962 Light waves at the boundary of nonlinear media. *Phys. Rev.* **128**, 606–622. (doi:10.1103/PhysRev.128.606)
43. Liu X, Tang T, Mostert W, Adcock TAA. 2025 Phase manipulation to analyse different types of nonlinearity using water waves as a case study. Zenodo. (https://doi.org/10.5281/zenodo.15002658)